IPP-Report

Max-Planck-Institut für Plasmaphysik

Tanja Geib

Beam Tracing Simulations for ITER-Reflectometry

IPP 5/132
August, 2012

Technische Universität München

Department of Physics

Bachelor's Thesis

Beam-Tracing Simulations for ITER-Reflectometry

Tanja Geib

performed at the **Max Planck Institut für Plasmaphysik (IPP)**

Supervisor: Prof. Sibylle Günter

Advisors: PD Dr. Emanuele Poli, Dr. Garrard Conway, Andreas Stegmeir

Submission Date: July 25, 2012

Acknowledgements

Zu Beginn möchte ich mich herzlich bei all den Menschen bedanken, die mich in den letzten drei Monaten so tatkräftig unterstützt und so diese Arbeit ermöglicht haben. Zunächst möchte ich Frau Prof. Dr. Sibylle Günter für die Möglichkeit danken, meine Bachelorarbeit am IPP durchzuführen, sowie für die Vermittlung bei der Suche nach einem passenden Thema. Ein riesengroßes Dankeschön geht an meine drei Betreuer: Emanuele, Danke für die freundliche Aufnahme am IPP, die Einführung in die Plasmaphysik, und die Anleitung und Betreuung während allen Etappen meiner Bachelorarbeit. Danke, für all die Zeit, die du dir für Fragen und Korrekturen genommen hast und dafür dass deine Tür wirklich immer offen steht. Garrard, I want to thank you for the introduction into reflectometry, all the ideas and input you contributed to this work. Especially, I thank you for spending your time on showing me how to make results presentable. Und last but no least: Andi. Danke für die moralische Unterstützung und permanente Betreuung während meiner gesamten Zeit am IPP. Danke für die Einarbeitung und Betreuung bei der Arbeit mit dem Code, sowie sämtliche Unterstützung bei der Arbeit mit Programmen jeglicher Art. Dank dir, hat sich so manch ein störrischer Scan ergeben und sich so einige Fragezeichen bezüglich der Theorie in 'Aha'-Erlebnisse verwandelt. Danke für die Graphen, die du für diese Arbeit bereitgestellt hast, für alle Ermunterungen und dass du immer ansprechbar warst.

As well, I want to warmly acknowledge Fusion for Energy (Mario Cavinato) for making the equilibria produced under Grant 255 (Self-consistent simulation of plasma scenarios for ITER) available to us.

Zu guter Letzt möchte ich meiner Familie und meinen Freunden danken. Mit euch kann man jede Lebenslage teilen. Danke! Vorallem danke ich meinen Eltern, dass sie mir so treu mit Rat und Tat zur Seite stehen. Und meiner Tante Bärbel, die mich fortwährend unterstützt.

Contents

Chapter 1

Introduction and Theoretical Background

1.1 Outline

The subject of this thesis is the measurement of the density in a plasma under conditions typical of a tokamak nuclear fusion reactor. The diagnostic technique considered here is called microwave reflectometry and is based on the reflection of an electromagnetic wave beam. The information about the plasma density is inferred from the detection of the beam after reflection by the plasma. For the International Thermonuclear Experimental Reactor (ITER), presently under construction, the parameters of the reflectometry system are being disucussed. In the present work, the optimization of the proposed ITER low-field-side reflectometer system is investigated. Furthermore, this system is analyzed with particular reference to its performance during the evolution of a typical (simulated) ITER plasma discharge. Chapter 1 introduces the theoretical basics of fusion in a tokamak reactor, of wave propagation in a plasma and of the diagnostic technique reflectometry. Chapter 2 connects this with the current ITER configuration, previous investigations and the present optimization process on low-field-side reflectometers, as well as with the new opportunity of investigating the whole evolution of a ITER plasma discharge. Chapter 3 presents the results of this work.

1.2 Nuclear Fusion

In search of new powerful and sustainable energy sources, a promising approach is the controlled realization of nuclear fusion processes on Earth. Basically there are two ways to gain energy from a nuclear reaction: nuclear fission and nuclear fusion. Fission occurs only

for nuclei that are heavier than iron. The binding energy per nucleon of the nuclear parent has to be lower than the binding energy per nucleon of the fission products. The energy difference is released. In fusion, light nuclei join together and form a heavier nucleus. Again the binding energy per nucleon increases through the reaction. In both cases matter is not conserved but rather converted into energy. Fig. 1.1 illustrates this principle.

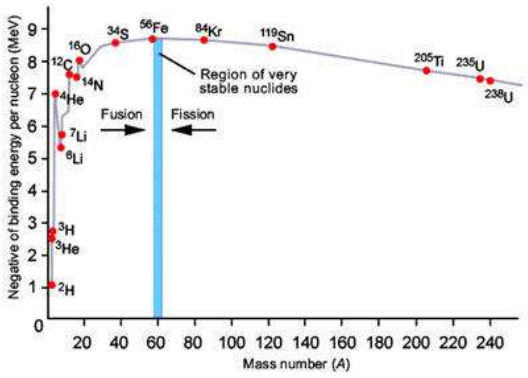

Figure 1.1: Binding energy per nucleon as a function of mass number A

Nuclear fusion is for example observed in the Sun. The process taking place on the Sun, called proton-proton chain [1], fuses four hydrogen nuclei in several steps into one helium nucleus. However, the deuterium-tritium fusion has the highest cross section while requiring comparatively small particle energies [2]:

$$ {}^{2}_{1}D + {}^{3}_{1}T \rightarrow {}^{4}_{2}He(3,5\ MeV) + {}^{1}_{0}n(14,1\ MeV). \tag{1.1} $$

Each fusion reaction releases 17,6 MeV. When two nuclei fuse they need to overcome the electric repulsion caused by the Coulomb force. Thanks to the quantum mechanical tunnel effect, this is also possible for energy differences smaller than the Coulomb barrier. It is however not possible to achieve fusion by shooting deuterium ions on a tritium target because the cross section for fusion is a lot smaller than it is for elastic collisions. It is essential that the constituents of fusion are at a temperature at which the reaction rate is high enough and an adequate number of nuclei fuse. This is the case at temperatures above 10 keV where reactants exist in a plasma state, which means that matter is mostly ionized.

To finally run a fusion reactor that produces usable energy the plasma has to reach, or at least approach, ignition. Ignition means that the heating by the α-particles is sufficient to maintain the temperature of the plasma against dissipation losses without using external power input. To reach ignition, a plasma has to fulfill the Lawson criterion, which requires that the plasma heating through α-particles is larger that the losses due to radiation and transport. In case of a deuterium-tritium fusion in a tokamak the condition for ignition is [3]:

$$n\tau_E T \geq 3 \cdot 10^{21} m^{-3} keVs, \tag{1.2}$$

where τ_E is the confinement time which measures the rate at which the plasma loses energy to its environment, n is the density and T the temperature of the plasma. There are two concepts accomplishing the condition for ignition. For inertial confinement fusion, one achieves a very high density over a short period of time by heating and compressing a fuel target. In magnetic confinement fusion, fusion is achieved through longer confinement times ($\tau_E \approx 3$ s) and lower densities ($n \approx 10^{20}$ m^{-3}). The reactor ITER, aiming at demonstrating the possibility of energy gain through controlled nuclear fusion, is based on magnetic confinement, which is discussed in the following section.

1.3 Tokamak Physics

As mentioned above, it is essential to confine the plasma in order to achieve the conditions for producing electrical power from thermonuclear fusion. Fusion plasmas are at a temperature above 100 million degrees Celsius (> 10 keV). As a consequence, it is impossible to confine the plasma in material vessels without re-cooling the plasma. Instead one takes advantage of the fact that in a plasma matter is ionized and therefore its particles respond to magnetic and electric fields. A homogeneous magnetic field forces charged particles to move on helical paths around the field lines. Consequently ions and electrons can move freely alongside the magnetic field lines whereas their motion is restricted radially. A first idea to confine a plasma using a magnetic field would be to bend a cylinder into a torus. Thus the axial magnetic field becomes toroidal. Thereby one achieves a spatially limited configuration. However, this configuration including only a toroidal magnetic field does not provide a confined plasma. The toroidal magnetic field is inversely proportional to the distance to the symmetry axis of the torus. That causes the field to decrease by moving away from the rotation axis or in other words, the toroidal field possesses a gradient directed towards the torus axis. This gradient together with the curvature of the toroidal field leads to a vertical drift of the charged particles which is directed up or downwards depending on the sign of their charge. Eventually, this charge separation causes a vertical electric field that makes the electrons and ions drift outwards so that the plasma cannot be confined by this configuration. To effectively confine a plasma in a toroidal configuration one possibility is to use a poloidal magnetic field which is generated by a toroidal current inside the plasma. Together with the toroidal magnetic field this leads to twisted magnetic field lines which prevent the plasma from drifting. This configuration is used in a tokamak (from Russian 'toroidal chamber with magnetic field'), see figure 1.2.

Through this configuration the twisted magnetic field lines set up toroidal nested magnetic surfaces. On these surfaces, also called flux surfaces, the plasma pressure outwards is compensated by a pressure caused by the magnetic field. On a magnetic surface, pressure, as

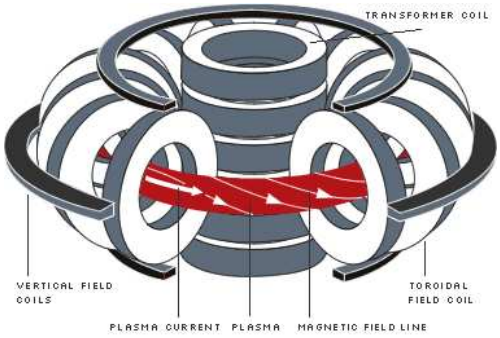

Figure 1.2: Magnet system of tokamak fusion device

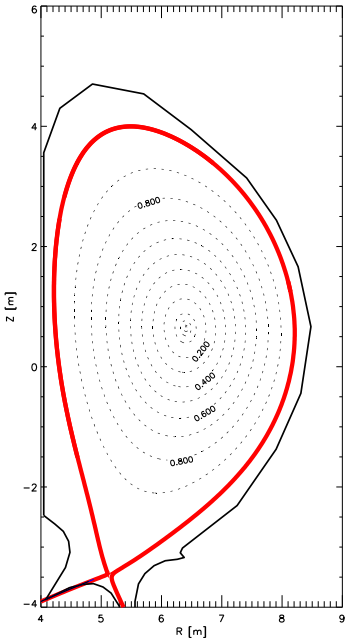

Figure 1.3: Transverse section of ITER plasma at the end of burn phase

well as density and temperature are constant. In a tokamak a third, vertical field generated by external ring coils fixes the position as well as the form of the plasma.

The transversal section of a tokamak is shown in figure 1.3 for the case of ITER at the end of the nuclear burn phase. The thick red line separates closed from open field lines thus limits the plasma and is called separatrix. The dashed lines represent the magnetic surfaces which are labeled by the normalized radius ρ. The magnetic axis, i.e. the centre of the plasma 'column', is identified by $\rho = 0$, whereas $\rho = 1$ indicates the separatrix. Density and temperature usually attain their maximum value on the magnetic axis, as depicted in Fig. 1.4, for the ITER equilibrium of Fig. 1.3. The density profile displays a steep edge, called the pedestal region, typical of the high energy/particle confinement H-mode operation.

1.4 Wave Propagation in a Plasma

Since the propagation of electromagnetic waves in a fusion plasma plays a major role in this thesis, some fundamental aspects are summarized here. See [4] for more details.

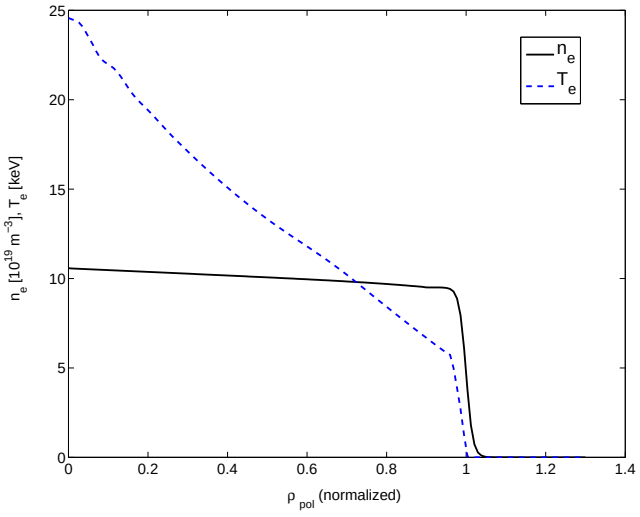

Figure 1.4: Density and temperature profile as a function of poloidal radius for ITER at the end of the burn phase

1.4.1 Basics

The propagation of an electromagnetic wave is described by Maxwell's equations (here in Gaussian units), see Eq. 1.3 to Eq. 1.6. A plasma consists of charged particles, therefore its interaction with an electromagnetic wave is very complex. Furthermore, a tokamak plasma is an inhomogeneous medium that causes the wave vector to vary during the propagation through the plasma. For magnetic fields are applied to the plasma in a tokamak configuration, it is no longer an isotropic medium but becomes anisotropic.

$$\nabla \cdot \vec{E} = 4\pi\rho \tag{1.3}$$

$$\nabla \cdot \vec{B} = 0 \tag{1.4}$$

$$\nabla \times \vec{E} = -\frac{1}{c}\frac{\partial \vec{B}}{\partial t} \tag{1.5}$$

$$\nabla \times \vec{B} = \frac{1}{c}\frac{\partial \vec{E}}{\partial t} + \frac{4\pi}{c}\vec{J} \tag{1.6}$$

So, to describe the propagation of an electromagnetic wave in a typical fusion plasma the equation to solve is given by Eq. 1.7, which is obtained from Eq. 1.5 and Eq. 1.6, assuming a temporal dependence $\vec{E} \propto e^{-i\omega t}$.

$$\frac{c^2}{\omega^2}\nabla\times(\nabla\times\vec{E})-\epsilon\cdot\vec{E}=0 \tag{1.7}$$

In this equation, ϵ is the dielectric tensor. For its explicit derivation, see [5].

There are two assumptions for a beam propagating through a tokamak plasma that simplify Eq. 1.7 essentially. First of all, for microwave or mm-wave beams in a typical fusion plasma, the condition that the radiation wavelength λ of the launched electromagnetic wave is much smaller than the inhomogeneity scale L of the plasma is satisfied. Secondly, the beam launched into the plasma is localized in a region of width $w \ll L$ around the beam axis. Under these assumptions, an approach, called Beam Tracing Theory, is made to solve 1.7 by approximation which will be discussed in subsection 1.4.3.

Another important consequence of the anisotropy of a tokamak plasma is that the polarization of a launched wave affects its propagation throughout the plasma. For an electromagnetic wave launched perpendicular to the magnetic field there are two options, dependent on the possible orientation of the wave field:

O-mode An O-mode wave is transverse polarized parallel to the magnetic field applied to the plasma. That means that the particles oscillate in the electric field of the wave parallel to the magnetic field. Consequently, no Lorentz force is applied and the wave propagates like in an unmagnetized plasma. The refractive index N only depends on the frequency of the probing beam ω and the electron density n_e and has the form:

$$N^2=1-\frac{\omega_{pe}^2}{\omega^2}. \tag{1.8}$$

X-mode For the X-mode, polarization is perpendicular to the magnetic field which means that particles oscillate perpendicular to the magnetic field. In this case, the refraction index additionally depends on the magnetic field:

$$N^2=1-\frac{\omega_{pe}^2}{\omega^2}-\frac{1}{A}\frac{\omega_{pe}^2}{\omega^2}\frac{\omega_{ce}^2}{\omega^2}. \tag{1.9}$$

with $A=1-\frac{\omega_{pe}^2}{\omega^2}-\frac{\omega_{ce}^2}{\omega^2}$.

The plasma density and the magnetic field determine the refractive index through the plasma frequency ω_{pe} and the cyclotron frequency ω_{ce}.

Plasma frequency A tokamak plasma is a quasi-neutral gas of positively charged ions and negatively charged electrons. Small displacements of electrons with respect

to the ions cause a Coulomb force to act between the charged particles. This leads to an oscillation of the electrons with respect to the heavier ions. The frequency at which electrons oscillate around ions is called (electron) plasma frequency, $\omega_{pe} = \sqrt{\frac{4\pi n_e e^2}{m}}$ (e the electron charge, m the electron mass).

Cyclotron frequency In a magnetic field, electrons orbit the magnetic field lines with a frequency $\omega_{ce} = \frac{eB}{mc}$, which is the (electron) cyclotron frequency.

In the following, an import role is played by the cutoff frequency.

Cutoff frequency A wave propagating through a magnetized plasma can encounter a cutoff, generally defined as the position at which the refractive index N goes to zero. Near the cutoff, the wave is reflected. If an O-mode beam is launched into a fusion plasma at a fixed frequency ω, it passes through increasing densities as long as the frequency of the beam is higher than the plasma frequency ω_{pe}. The plasma frequency increases with the density. If it reaches a point where $\omega = \omega_{pe}$, there N vanishes and the beam is reflected. In the case of an X-mode, the dispersion relation is more complex and there are two cutoff frequencies at $\omega = \sqrt{(\frac{\omega_{ce}}{2})^2 + \omega_{pe}^2} \pm \frac{\omega_{ce}}{2}$.

In this thesis, the injection of microwave beams for diagnostic purposes is investigated. That means that the impact of the plasma on the electromagnetic wave is used to gain information about structure and processes inside a plasma, see section 1.5. Thereby, the electromagnetic wave is modeled as a Gaussian Beam. This is further described in the following subsection.

1.4.2 Gaussian Beam

The Gaussian Beam is a concept in ray and wave optics to describe a radiation field whose transverse amplitude profile is a Gaussian curve [6].

The behavior of a Gaussian beam can be described using several parameters which will be explained in the following with the aid of Fig. 1.5. In the following considerations, it is assumed that the beam propagates parallel to the $z-$axis and its waist is at the origin of the $z-$axis.

The beam width $w(z)$, see Eq. 1.10 below, is defined as the distance from the propagation axis at which the intensity drops to $1/e^2$ of the maximum value. The minimum of the beam width is called beam waist w_0. The formula describing the dependence of the beam width on the axial distance z in vacuum is:

$$w(z) = w_0 \sqrt{1 + \frac{z^2}{z_R^2}}. \tag{1.10}$$

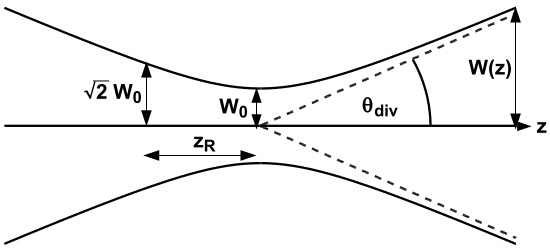

Figure 1.5: Schematic of a Gaussian Beam showing the beam waist w_0, the beam width $w(z)$ as a function of axial distance z, the Rayleigh length z_R and the angular divergence θ_{div}

The distance along the propagation from the waist to the $z-$value where the cross section of the beam is doubled is called Rayleigh length z_R. The Rayleigh length is given by $z_R = w_0^2\omega/2c$ and corresponds to the beam width $w(\pm z_R) = w_0\sqrt{2}$.

The parameter $R(z)$, see Eq. 1.11 below, called radius of curvature, describes the form of the phase front, i.e. the focusing or de-focusing of the beam. At the beam waist, $z = 0$, the wave front is flat and R diverges

$$R(z) = z\left(1 + \frac{z_R^2}{z^2}\right). \tag{1.11}$$

At large distances $z \gg z_R$, $w(z)$ approaches a straight line. As a consequence $w(z)$ and $R(z)$ can be approximated by $w(z) \approx z\tan\theta_{div}$ and $R(z) \approx z$. The divergence of the beam θ_{div} is given by the angle between this straight line an the propagation axis:

$$\theta_{div} = \arctan\left(\frac{w_0}{z_R}\right). \tag{1.12}$$

The total angular spread is given by $\Theta = 2\theta_{div}$.

1.4.3 Beam-Tracing Theory

In Beam Tracing Theory [7, 8, 9, 10], the propagation of a Gaussian Beam is described by the propagation of its central axis as well as the evolution of both the curvature of the phase front and the width of the beam. Like in Ray Tracing, the mostly known approach of geometrical optics, Maxwell's equations are reduced to a set of ordinary differential equations. In Beam Tracing, however, diffraction effects perpendicular to the central axis are explicitly taken into account. This section summarizes the basic idea and results of the Beam Tracing Theory and its relation to the parameters of a Gaussian Beam.

To solve Eq. 1.7, the electromagnetic wave is expressed in the form:

$$\vec{E}(\vec{r}) = \vec{A}(\vec{r}) \exp\left[i(s(\vec{r}) + i\phi(\vec{r}))\right]. \tag{1.13}$$

where $\vec{A}(\vec{r})$ is the amplitude and $\overline{s}(\vec{r}) = s(\vec{r}) + i\phi(\vec{r})$ is the complex phase of the wave. $s(\vec{r})$ is connected with the phase of the beam, $\phi(\vec{r}) \geq 0$ describes its transverse structure, that is to say its cross section. As mentioned in subsection 1.4.1, for mm-waves in fusion plasmas, the plasma inhomogeneity is weak and the beam width is limited, so that $\lambda \ll w \ll L$ is satisfied. This allows us to expand the complex phase $\overline{s}(\vec{r})$ up to second order around the central axis of the beam:

$$s(\vec{r}) = s_0(\vec{r}) + K_\alpha \left[x_\alpha - q_\alpha\right] + \frac{1}{2} s_{\alpha\beta} \left[x_\alpha - q_\alpha\right] \left[x_\beta - q_\beta\right], \tag{1.14}$$

$$\phi(\vec{r}) = \frac{1}{2} \phi_{\alpha\beta} \left[x_\alpha - q_\alpha\right] \left[x_\beta - q_\beta\right], \tag{1.15}$$

where q_α are the components of the position vector $\vec{r} = \{x_\alpha\}$ and $K_\alpha = \nabla s$ are the components of the wave vector $\{k_\alpha\}$, respectively, at the central ray of the Gaussian Beam. The second-order parameters of Eq.1.14 and Eq.1.15, the so called Beam matrices, $s_{\alpha\beta}$, which is related to the curvature R of the phase front, and $\phi_{\alpha\beta}$, which is related to the width w of the beam, as well as the quantities K_α and q_α are obtained by solving the beam tracing equations:

$$\frac{dq_\alpha}{d\tau} = \frac{\partial H}{\partial k_\alpha} \tag{1.16}$$

$$\frac{dK_\alpha}{d\tau} = -\frac{\partial H}{\partial x_\alpha} \tag{1.17}$$

$$\frac{ds_{\alpha\beta}}{d\tau} = \left(-\frac{\partial^2 H}{\partial x_\alpha \partial x_\beta} - \frac{\partial^2 H}{\partial x_\beta \partial k_\gamma} s_{\alpha\gamma} - \frac{\partial^2 H}{\partial x_\alpha \partial k_\gamma} s_{\beta\gamma} - \frac{\partial^2 H}{\partial k_\gamma \partial k_\delta} s_{\alpha\gamma} s_{\beta\delta} + \frac{\partial^2 H}{\partial k_\gamma \partial k_\delta} \phi_{\alpha\gamma} \phi_{\beta\delta} \right) \Bigg|_{x_\alpha = q_\alpha, k_\alpha = K_\alpha} \tag{1.18}$$

$$\frac{d\phi_{\alpha\beta}}{d\tau} = \left(-\left(\frac{\partial^2 H}{\partial x_\alpha \partial k_\gamma} + \frac{\partial^2 H}{\partial k_\gamma \partial k_\delta} s_{\alpha\beta} \right) \phi_{\beta\gamma} - \left(\frac{\partial^2 H}{\partial x_\beta \partial k_\gamma} + \frac{\partial^2 H}{\partial k_\gamma \partial k_\delta} s_{\beta\delta} \right) \phi_{\alpha\gamma} \right) \Bigg|_{x_\alpha = q_\alpha, k_\alpha = K_\alpha}. \tag{1.19}$$

It is noted that Eq.1.16 and Eq. 1.17, describing the evolution of the central ray, are Hamiltonian equations as known from standard geometrical optics. In the previous equations, the

Hamiltonian function H is the dispersion function, which can be deduced by substituting Eq. 1.13 into Eq. 1.7 and retaining terms to the lowest order in $\frac{\lambda}{L}$ only:

$$H := det\left[\left(\frac{c}{w}\right)^2\left(-k^2\hat{I}+\vec{k}\vec{k}\right)+\epsilon^h\right]=0, \tag{1.20}$$

with ϵ^h is the Hermitian part of the dielectric tensor (the anti-Hermitian part of ϵ does not play any role in the present study).

A beam that is launched into an anisotropic plasma evolves with an anisotropic cross section. It is described as an ellipse. After solving the beam tracing equations, one can use the eigenvalues of $\phi(r)$ in a plasma perpendicular to the propagation direction to describe the principal widths of the beam:

$$w_{maj}(r)=\sqrt{\frac{2}{\min\left(\phi_1(r),\phi_2(r)\right)}} \qquad w_{min}(r)=\sqrt{\frac{2}{\max\left(\phi_1(r),\phi_2(r)\right)}}. \tag{1.21}$$

The orientation of the ellipse also can be calculated from the eigenvalues. This shows that a launched Gaussian beam gets modified by the tokamak plasma in a way that its cross section, called footprint, gets deformed and rotated. This evolution can be calculated once the dispersion relation and the initial conditions of the Gaussian Beam are known. An example of this process is shown in Fig. 2.3.

This process of solving the beam tracing equations is performed numerically by the TORBEAM code [11]. As an input, experimental magnetic equilibria as well as density and temperature profiles are used. The code is complemented by a generalized Snell's Law to describe the transition from vacuum into the plasma (and vice versa) and a relativistic mass correction which leads to an approximated effective mass in the dielectric tensor [12]. Further through this thesis the cutoff will be of significance. While the approximations, which led to the beam tracing approach, are satisfied for most of the path the propagation through a plasma, they break down close to the cutoff. However, comparing positions of the cutoff in full-wave simulation and beam tracing simulation shows that the beam tracing solution is close enough to the exact solution [13, 14]. That enables the use of TORBEAM for reflectometric analysis.

1.5 Reflectometry

Reflectometry is a microwave radar based diagnostic which can be used to measure: 1. electron plasma density profiles, 2. density fluctuations and structure and 3. plasma rotation via Doppler shifts (for general information on reflectometry, see [15], for more specific disquisitions, see [16, 17, 18]).

Fig. 1.6 shows a schematic of a simple microwave reflectometer circuit. A beam is launched into the plasma from a transmit (T_x) horn antenna, reflected at the plasma cutoff, like on a mirror, and received by a second antenna (R_x). The received signal is mixed with a reference signal (derived from the launched signal) to produce a 'video' signal $A\cos\phi$, where ϕ is the relative phase shift related to the propagation path length d.

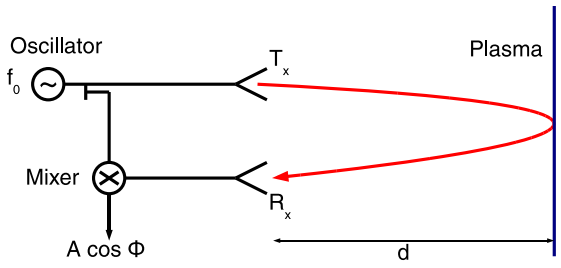

Figure 1.6: Schematic illustration of a microwave reflectometer curcuit

In a radar, the phase delay is directly proportional to the distance of the cutoff. However, in the case of plasma, the wave propagates through a medium whose refractive index $N \neq const$, see Fig. 1.7.

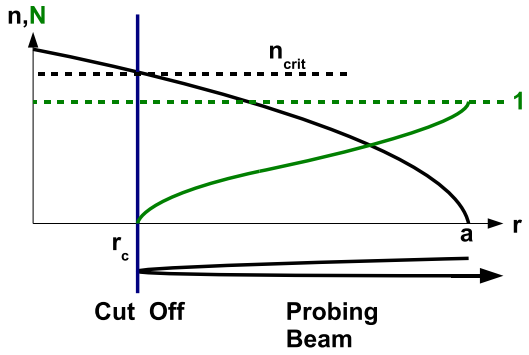

Figure 1.7: Principle of reflectometry, with n as density and N as refractive index

Based on geometrical optics, the phase delay of a beam propagating in between to points A and B is given by

$$\triangle\,\phi(B) - \triangle\,\phi(A) = \frac{\omega}{c}\int_A^B N(r)\,dr, \tag{1.22}$$

where $N(r)$ is the refractive index as a function of the radial coordinate r. In the case of an O-mode beam the phase delay between the forward and reflected beam is given by

$$\triangle \phi = \frac{2}{c} \int_{r_c}^{a} \sqrt{\omega^2 - \omega_p^2(r)}\, dr - \frac{\pi}{2}, \tag{1.23}$$

which includes the phase change of $\pi/2$ at the reflection layer. By sweeping the launch frequency f_0, different cutoff layers can be probed and the density profile can be reconstructed using an Abel inversion algorythm.

Open-ended corrugated waveguides serve as antennas. In ITER, frequency ranges about 18 to 80 GHz for the O-mode and 120 to 160 GHz for the X-mode are planned. To avoid great losses and to cover the aimed frequency ranges, antenna diameters planned for ITER are: $D_O = 63.5$ mm for the O-mode and $D_X = 31.75$ mm for the X-mode [19]. The beam launched by the antenna is modeled as a Gaussian Beam, see Fig. 1.8 (which is a very good approximation for the real beam), with the following initial conditions: the wave front is flat and the cross section circular, given by $w_0 = 0.32D$. Again the width of the beam as well as its curvature evolve in vacuum according to Eq. 1.10 and Eq. 1.11. Its divergence is given by Eq. 1.12. This shows that $\theta_{div} \propto \frac{1}{\omega D}$, which means that the lower the frequency ω and the smaller the diameter D the more the beam expands.

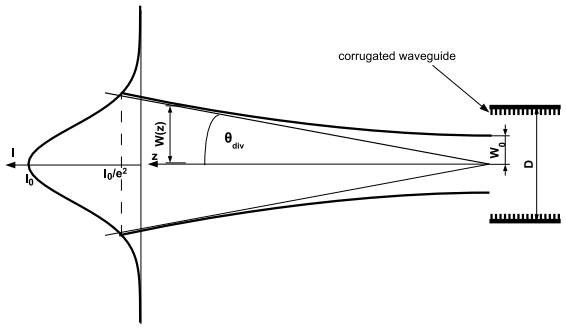

Figure 1.8: Radiation of the beam from the antenna in vacuo

The signal power is as well expressed in terms of the antenna gain [21]:

$$G = \frac{4\pi}{\lambda^2} A_{eff} \tag{1.24}$$

where $A_{eff} \propto \pi \left(\frac{D}{2}\right)^2$ is the effective antenna area and λ the probing radiation wavelength (with $\lambda = \frac{2\pi c}{\omega}$).

After propagating through the plasma, the reflected beam hits the receiver antenna. The signal power depends on how well the beam couples with the receiver. The coupling coefficient T_a depends on the size of the footprint as well as on its incidence angle θ_{inc} and the offset of its central ray, see Fig. 1.9. To obtain good coupling, the footprint of the reflected beam has to be big enough to overlap with the antenna radiation pattern, but small enough

so that the intensity is not spread too much. Furthermore, for good coupling the phase front should be parallel to the receiver antenna waveguide front. As soon as the incident angle is bigger than the beam divergence, see Eq. 1.12, the power, coupled into the antenna, drops abruptly. Thus, the alignment of the antenna line-of-sight with the cutoff is crucial for good performance of the diagnostic.

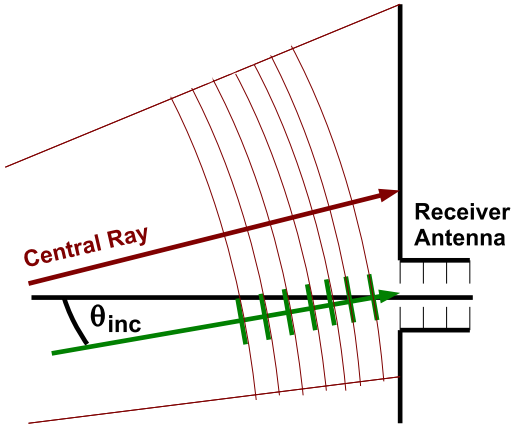

Figure 1.9: Schematic illustration of the incident reflected beam into the receiver antenna

An explicit evaluation of the coupling efficiency T_a can be performed within the frame of the beam tracing theory according to the formula derived in [20].

Chapter 2

Overview of Previous Results

The aim of this thesis is to investigate: 1. the degree of antenna tilting range required to compensate the vertical plasma column movements and 2. the degree of beam alignment variation during the plasma ramp-up. This chapter summarizes previous results and gives an introduction to the subject investigated in chapter 3.

2.1 ITER Configuration

For ITER, various reflectometer systems are planned. Fig. 2.1 illustrates a poloidal cross section of the ITER tokamak (with the major $R_0 = 6.2$ m, the minor radius $a = 2.0$ m, the toroidal magnetic field $B_t = 5.3$ T, and the plasma current $I_p = 15$ MA) including proposed positions for the reflectometer systems [22]. For this thesis, the Low-Field-Side (LFS) systems are of interest (LFS-O, LFS-XR). The port-plug of such a Low-Field-Side Reflectometer is showed in Fig. 2.2.

Since several different diagnostic devices will share a port, it is important to consider the alignment and placement of the systems well. The investigated LFS antenna device is expected to operate over frequency ranges of 18-80 GHz for the O-mode polarization and over 120-160 GHz for the X-mode polarization and allow, principally, an investigation of the edge plasma density region. Respectively, the low frequency probing beams, 18 GHz and 120 GHz, are reflected in the scrape-off layer of the plasma, while the probing frequencies at 60 GHz and 140 GHz are reflected in the middle of the pedestal and the 80 GHZ and 160 GHz frequency beams at the top of the pedestal.

For the design, there are several degrees of freedom available:

- Monostatic or bistatic: In a monostatic configuration, the launch antenna is used as receiver, too. A bistatic system has separate antennas for launching and receiving.

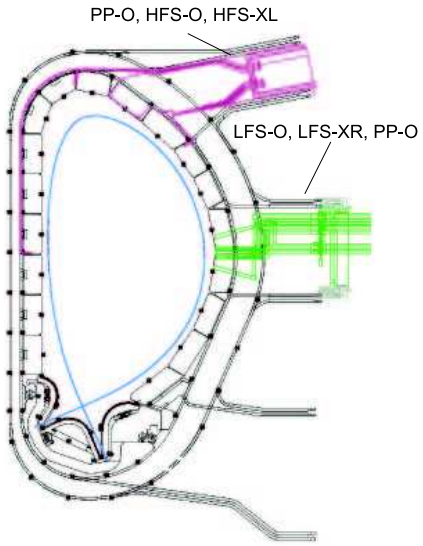

Figure 2.1: Poloidal cross section of ITER showing locations of reflectometer systems: Plasma Position (PP) and High Field Side (HFS) systems (purple), PP and Low-Field-Side (LFS) systems (green). The LFS-O and LFS-XR are discussed here.

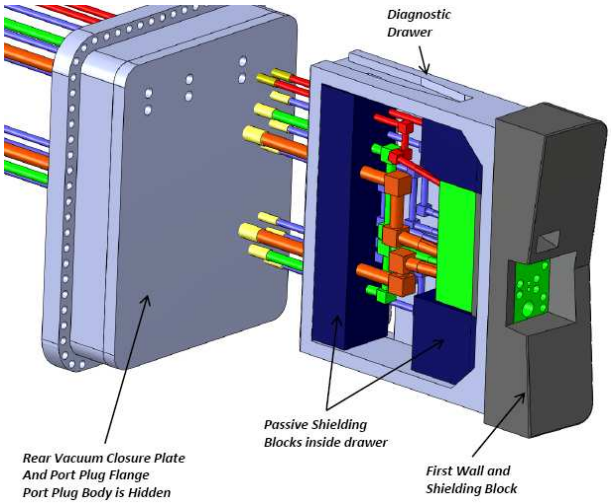

Figure 2.2: Port plug design for a LFS system for ITER

Both systems do have advantages and disadvantages that are discussed for example in [24].

- Number of antennas: In general, the more antennas available the better, as the system is more robust and more flexible. However, one has to bear in mind that the port is used by other diagnostic devices as well and consequently space is limited.

Furthermore, the number may be restricted by economic reasons.

- Antenna position: Basically, it is possible to position the antennas vertically anywhere in the port space, as well as to recess them, as far as the port allows it. The limits, in this case, are with respect to the coupling efficiency.
- Antenna diameter: The antenna diameter defines the antenna gain. Throughout this thesis, the diameters were fixed at the current design values [19].
- Antenna tilt: The antenna can be tilted in toroidal and poloidal directions to improve the coupling by changing the incidence angle of the beam on the plasma cutoff layer.

2.2 Previous Results

The parameters above have already been subject to several investigations. Before discussing the previous results, the figure below will help to illustrate, how the beam propagation and reflection within the ITER tokamak works.

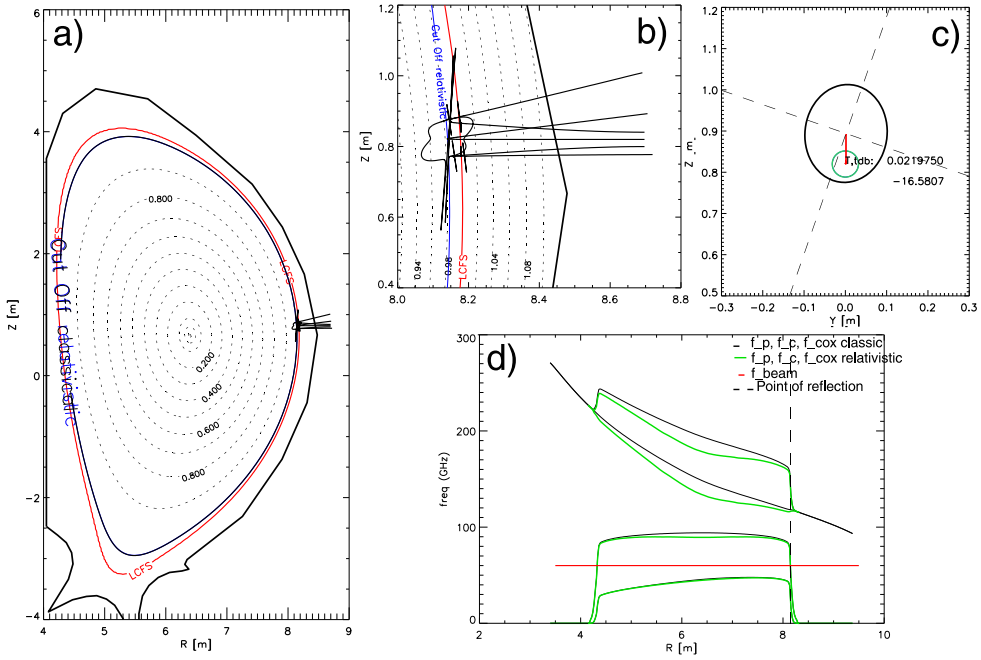

Figure 2.3: a) Polodial cross section of the ITER tokamak with propagation of a 60 GHz O-mode beam at the end of the burn phase. b) Cutout of the area of reflection seen in a). c) Toroidal view on the launched (green) and reflected (black) beam footprint. d) Cutoff frequency profile of the plasma as a function of the radius R at the height of the magnetic axis. The upper curve is the upper X-mode cutoff, the second one is the cyclotron frequency, the third one is the O-mode cutoff (plasma frequency) and the fourth one the lower X-mode cutoff (black: non-relativistic, green: including relativistic corrections).

In Fig. 2.3, a 60 GHz O-mode beam is launched from the middle of the port at $z_{ant} = 0.82$ m, $R_{ant} = 8.6978$ m and $\vartheta_{ant} = 0°$ at the end of the burn phase. Subfigure a) shows the poloidal cross section of the ITER tokamak and illustrates that the beam is reflected right after entering the plasma at the relativistic cutoff layer (blue). Subfigure b) shows the area of interest in a zoomed cutout. It can be seen, how the central ray as well as the beam width w evolve. Subfigure c) gives a toroidal view on the footprint of the launched beam in green as well as the footprint of the reflected beam in black. The red line shows how the central ray propagates looking at it from the position of the antenna throughout the whole propagation/reflection process. The value given in this subfigure is the coupling efficiency T_a. It is given in the units of dB, which is the logarithmic (to base 10) ratio of the power received to the power launched. Subfigure d) illustrates the relativistic cutoff frequencies (green) of the plasma as a function of the radius at the height of the magnetic axis. The red line gives the frequency of the launched beam. It can be seen that in this case the beam is reflected at the middle of the pedestal.

In the following, some results of previous investigations (see as well [23, 24, 25]) are mentioned:

Due to the varying refractive index, the beam drifts from its vacuum path and gets displaced. However, there is an antenna height z_{ant} where the propagation of the beam is purely radial. It was determined that this no-drift-height is at $z_{ant} = 0.62$ m [26, 20]. Also, there are vertical displacements of the plasma column during the plasma discharge. This vertical height variation of the magnetic axis is about $\Delta z = z_{ma} - z_{ant} = \pm 20$ cm [27]. The planned antenna designs are supposed to be able to handle these height variations. Another result of former examinations is that higher frequencies lead to greater offsets because the beam propagates further into the plasma before it is reflected. In general, one can express this as: the longer the path length the more the beam expands and is displaced. Therefore, recessing the antenna, as well, leads to a further spread of the reflected beam footprint. Current designs suggest a 20 cm recess of the antenna into the blanket module for thermal shielding [19]. Therefore, $R_{ant} = 8.6978$ m will be used as the initial point in this thesis.

Coupling is best for perpendicular launching without drift. Placing the antenna at $z_{ant} = 0.62$ m during the burn phase, consequently, provides the best coupling efficiency. In [26, 20], several different antenna systems including various antennas of fixed toroidal and poloidal tilt angles have been tested for their coupling efficiency in relation with their compensation of the plasma column height variation. It is important to notice that all former investigations were based on one equilibrium and that the vertical plasma column height variations were simulated by moving the antenna slightly up and down relative to the fixed equilibrium. Also, all results up to now were performed for a configuration corresponding to the ITER plasma at the end of the burn phase.

2.3 Subject of this Thesis

The results of this thesis extend the work summarized in the previous section and are subdivided into two parts. The first part is concerned with the ability of a single steerable antenna system to handle vertical plasma movements rather than the previously proposed vertical array of fixed tilt (i.e. horizontally aligned) antennas.

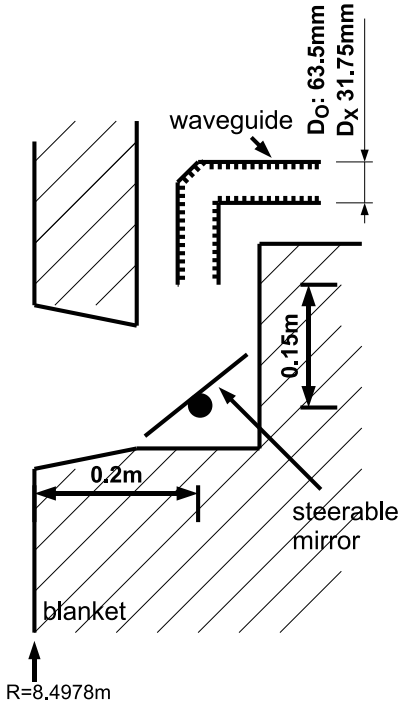

Figure 2.4: Schematic illustration of a possible implementation of a steerable antenna system

Fig. 2.4 shows a possible implementation of a poloidally steerable antenna system. Here, the corrugated waveguide antenna points downwards onto a steerable mirror element (flat or focusing), which deflects the beam radially inwards. Such a design is under consideration for the upper port ECRH steerable launcher [28]. The horn antennas are shielded within the blanket module to allow a degree of thermal shielding (as for previous proposed antenna systems [20]). In the design considered here, the mirror pivot point is recessed 20 cm from the blanket face and the horn some 15 cm vertically above. To simulate the horn-mirror geometry in the beam tracing, we replace the mirror with a tilted horn, recessed by an equivalent 35 cm. As well, it may also be possible for smaller tilt angles to simply mechanically tilt the waveguide at a 20 cm recess. Both options of steerable antenna designs are technically feasible and will be considered in section 3.1.

In the second set of results, LFS reflectometry for ITER is investigated considering several points in time during the plasma discharge. To this goal, we employ a new set of ITER equilibria [1] generated so as to cover the plasma discharge from current ramp-up through the flattop until the current ramp-down (see Fig. 3.8). This allows a study of the capabilities of the ITER reflectometers during the whole evolution of the plasma [2]. First scans are performed with a steerable antenna system, as in part one, to examine how much a fixed height, but steerable antenna system, as it is used for reflectometry at the end of the burn phase, would need to be tilted to track the evolution of the plasma during the ramp-up. The results are presented and discussed in section 3.2.

[1] These equilibria were produced under Grant 255 (Self-consistent simulation of plasma scenarios for ITER) issued by Fusion for Energy, which is here warmly acknowledged for making them available to us.

[2] The simulated discharge refers to a so-called ITER 'standard' scenario, i.e. the scenario which should demonstrate the feasibility of controlled fusion with an energy gain (ratio between fusion energy and energy injected to heat the plasma) equal to 10

Chapter 3

Results and Assessment

3.1 Part One: The Steerable Tilt Antenna System

The design shown in Fig.2.4 could have toroidally separated transmit and receive antennas (e.g. a bistatic configuration) or a single combined launch and receive antenna (e.g. a monostatic configuration). In the following assessment, we consider, for simplicity, the simple monostatic configuration. However, the general behavior and conclusions drawn will apply equally to a bistatic configuration. As a starting point, the horn antenna diameters (prior to the mirror) were chosen to be $D_O = 63.5$ mm for the O-mode and $D_X = 31.75$ mm for the X-mode, based on the proposed optimal antenna gains for the fixed alignment concept [19].

To access the critical issue for the reflectometer's sensitivity to vertical displacements of the plasma column during the plasma discharge, which can lead to undesirable beam swinging, the relative vertical displacement $\Delta z = z_{ma} - z_{ant}$ is simulated by moving the antenna up and down, relative to the fixed equilibrium.

The antenna is aligned in the middle of the port at $z_{ant} = 0.62$ m. Around this position, the plasma column height variation of $\Delta z = \pm 0.2$ m [27] is simulated in steps of 0.1 m. At each fixed height, the poloidal angle is varied and the optimal poloidal tilt angle, i.e. the angle with the maximum coupling efficiency T_a, is determined. This was performed for the O-mode frequencies 18, 60 and 80 GHz, as well as for the X-mode frequencies 120, 140 and 160 GHz. The results are presented in Fig. 3.1 and Fig. 3.2. The scans were performed for both a 0.2 m recess, i.e. $R_{ant} = 8.6978$ m, and a 0.35 m recess, i.e. $R_{ant} = 8.8478$ m, for the 60 GHz O-mode and the 140 GHz X-mode case.

In Fig. 3.1, the optimal poloidal tilt angle ϑ_{opt} is plotted as a function of the height variation Δz for the 60 GHz O-mode beam for both recesses. The results for the 18 GHz and the 80 GHz O-mode beam are practically identical to those of the 60 GHz beam. At most, they

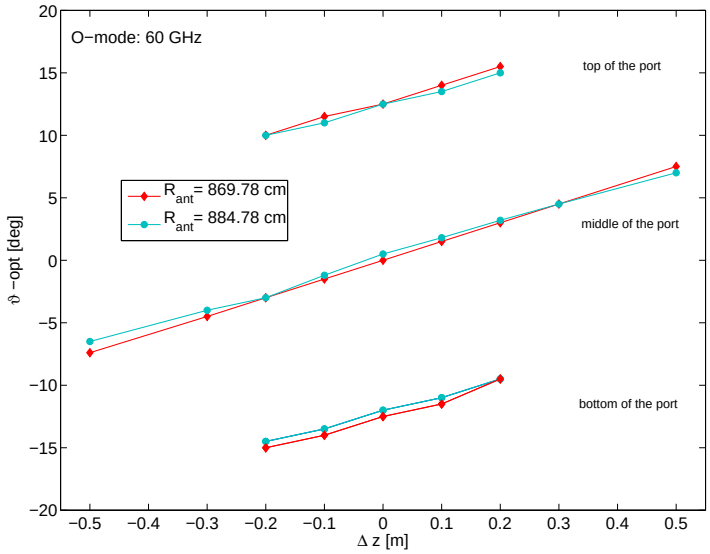

Figure 3.1: Optimal poloidal tilt angle ϑ_{opt} as a function of the height variation Δz for the 60 GHz O-mode beam at the middle ($z = 0.62$ m), the bottom ($z = -0.28$ m) and the top ($z = 1.52$ m) of the port for 0.20 m and 0.35 m recess antenna, i.e. $R_{ant} = 8.6978$ m and $R_{ant} = 8.8478$ m

differ only about ±0.2°. Also, the optimal tilt angles for the height variation $\Delta z = \pm 0.2$ m all lay between -3° and +3° and the dependence is roughly linear (for this equilibrium). To check the extent of this linearity, the height variation was increased to $\Delta z = \pm 0.5$ m. In principle, the antenna system could be placed anywhere within the port space. To check the effect of the antenna placement, the exercise is repeated with the antenna centred towards the top at $z_{ant} = 1.52$ m, and towards the bottom of the port at $z_{ant} = -0.28$ m. Height variation scans about $\Delta z = \pm 0.2$ m were performed for the 60 GHz O-mode beam and the results are presented in Fig. 3.1. Fig. 3.2 shows the results for the case of the X-mode beam at 140 GHz. Fig. 3.2, also, shows the optimal poloidal tilting behavior of the 120 GHz and the 160 GHz X-mode beam cases at the middle of the port.

Fig. 3.1 and Fig. 3.2 reveal various features: first, it is observed that the ϑ_{opt} variation with Δz for all three antenna positions are parallel, i.e. the optimal tilt angle reaction to the height variation Δz is independent of the antenna placement. This is due to the fact that the flux surfaces in front of the port, in which beams are reflected in this scenario, are only slightly, evenly curved. The general behavior is the same for all frequencies independent of the polarization. There is also no significant difference between the 0.2 m and 0.35 m recess. The optimal poloidal tilt angle range for height variations of $\Delta z = \pm 0.2$ m is -3° to 3° at the middle of the port, 9.5° to 15.5° at the top of port and -15.5° to -9.5° at the bottom of the port ('-' means tilting the antenna upwards, '+' means tilting it downwards). This means that, for each position of the antenna inside the port, the optimal tilt varies in

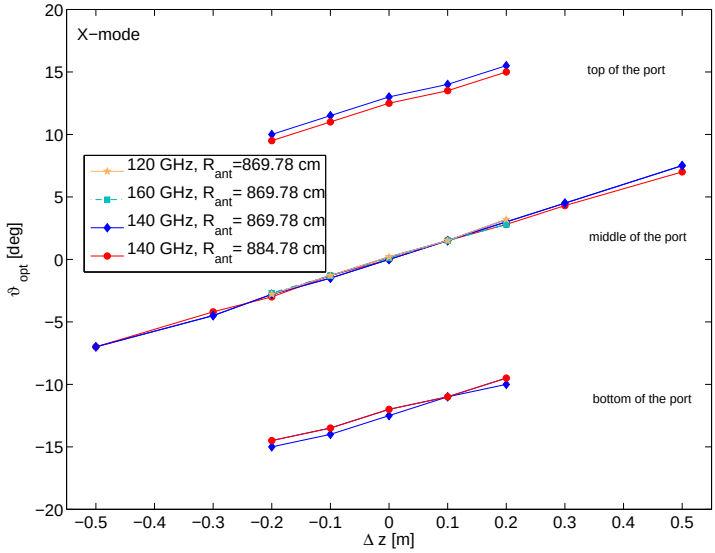

Figure 3.2: Optimal poloidal tilt angle ϑ_{opt} as a function of the height variation Δz for the 140 GHz X-Mode beam at the middle ($z = 0.62$ m), the bottom ($z = -0.28$ m) and the top ($z = 1.52$ m) of the port, as well as for the 120 and 160 GHz X-mode beam only at the middle of the port, for 0.20 m and 0.35 m recess antenna, i.e. $R_{ant} = 8.6978$ m and $R_{ant} = 8.8478$ m

between a $\pm 3^{\circ}$ range around the optimal tilt angle of the $\Delta z = 0$ position. In each case, the optimal tilting angle is reached when the central ray of the beam strikes the cutoff layer perpendicular, so that the central ray of the reflected beam hits the receiver antenna centre.

At the optimal poloidal tilt, the toroidal tilt was also varied. However, it showed that toroidal tilting with this antenna design does not improve the coupling efficiency significantly. Therefore, toroidal tilting was not considered further in this study.

The magnitude of the coupling efficiency T_a, its dependence on the antenna tilt and the sensitivity of the optimal tilt angle ϑ_{opt} are investigated next.

Fig. 3.3 shows the dependence of the coupling efficiency T_a on the poloidal tilt angle ϑ_{ant} for the O-mode beam frequencies 18, 60 and 80 GHZ at $R_{ant} = 8.6978$ m and $z_{ant} = 0.82$ m. The same was done in Fig. 3.4 for the X-mode beam frequencies 120, 140 and 160 GHz. The total value of the power coupling is -17.6 dB to -7.4 dB in O-mode and -16.8 dB to -13.1 dB in X-mode. These values are comparable to those obtained in previous studies [20]. Furthermore, especially for the O-mode polarization, the lower the frequency the less sensitive the coupling is to the tilt angle. This is due to the size of the footprint. As explained in section 1.5, at small frequencies the beam expands widely due to its stronger divergence. Since the intensity is spread over a large area, a good overlap is reached also

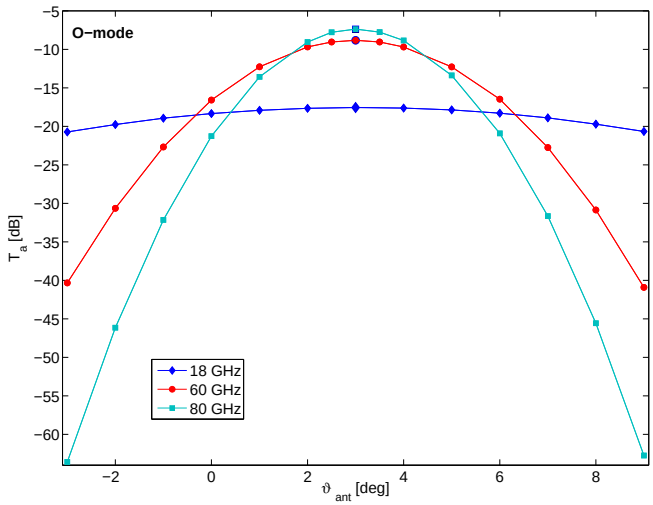

Figure 3.3: Coupling efficiency T_a as a function of the poloidal tilt angle ϑ_{ant} at $R_{ant} = 8.6978$ m and $z_{ant} = 0.82$ m (i.e. $\Delta z = +0.20$ m from the middle of the port) for the O-mode frequencies 18, 60 and 80 GHz

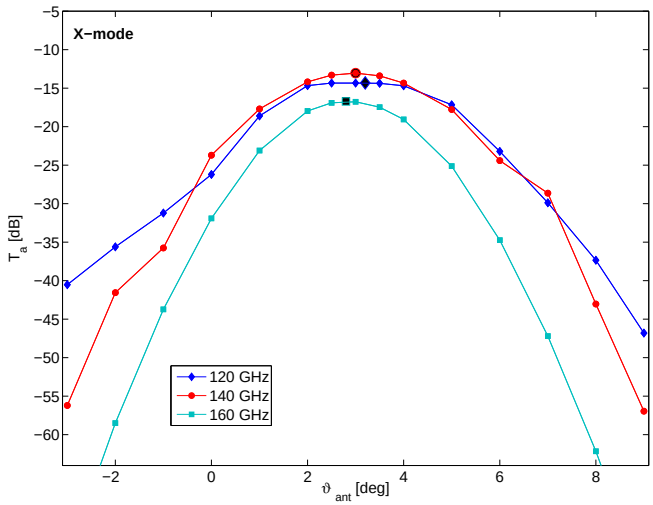

Figure 3.4: Coupling efficiency T_a as a function of the poloidal tilt angle ϑ_{ant} at $R_{ant} = 8.6978$ m and $z_{ant} = 0.82$ m (i.e.$\Delta z = +0.20$ m from the middle of the port) for the X-mode frequencies 120, 140 and 160 GHz

at a large tilt angle range but with a lower coupling. Comparing the two figures shows that the coupling dependence on the poloidal tilt angles is more sensitive at higher X-mode frequencies.

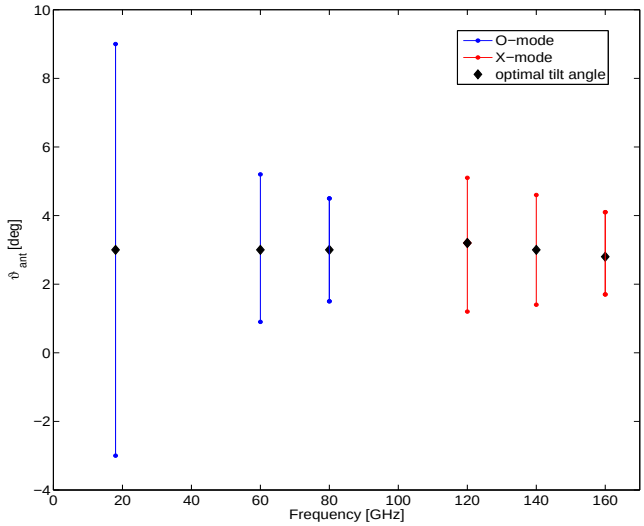

Figure 3.5: Range of the poloidal tilt angle ϑ_{ant}, in which the coupling efficiency T_a stays within a 3dB bar around the optimal coupling, as a function of the frequency at $R_{ant} = 8.6978$ m and $z_{ant} = 0.82$ m

In order to quantify the sensitivity of T_a on the tilt angle, Fig. 3.5 shows the ϑ_{ant} range where T_a drops by 3 dB as a function of the frequency for $R_{ant} = 8.6978$ m and $z_{ant} = 0.82$ m (i.e. $\Delta z = +0.20$ m from the middle of the port). A drop by 3 dB equals a reduction of the power received by the factor 2 and would be considered to be adequate for height variation compensation. Depending on polarization and frequency, the 3 dB width is between $\Delta\vartheta = 2°$ and $12°$. The behavior of Fig. 3.3 and Fig. 3.4 is emphasized: the lower the frequency, the less susceptible the coupling is to tilt angle variations. However, even for higher frequencies as 80 GHz O-mode and 160 GHz X-mode, a $\Delta\vartheta = 2°$ range provides acceptable performance for this antenna gain.

Fig. 3.6 and Fig. 3.7 replicate the behavior of Fig. 3.3 and Fig. 3.4 ($R_{ant} = 8.6978$ m and $z_{ant} = 0.82$ m) in more general terms. Here, T_a is plotted as function of the poloidal tilt angle ϑ_{ant} for a 60 GHz O-mode beam at $z = z_{ant} + \Delta z = 0.62$ m (middle of the port with $\Delta z = 0$), $z = 1.72$ m (top of the port with $\Delta z = +0.20$ m) and $z = -0.48$ m (bottom of the port with $\Delta z = -0.20$ m), and for $R_{ant} = 8.6978$ m (0.20 m recess), as well as for the mirror equivalent geometry $R_{ant} = 8.8478$ m (0.35 m recess) in Fig. 3.6 and for the 140 GHz X-mode beam in Fig. 3.7. In this exercise, the $z-$positions of the antenna where chosen to demonstrate the cases of the maximum Δz height variation at the top and

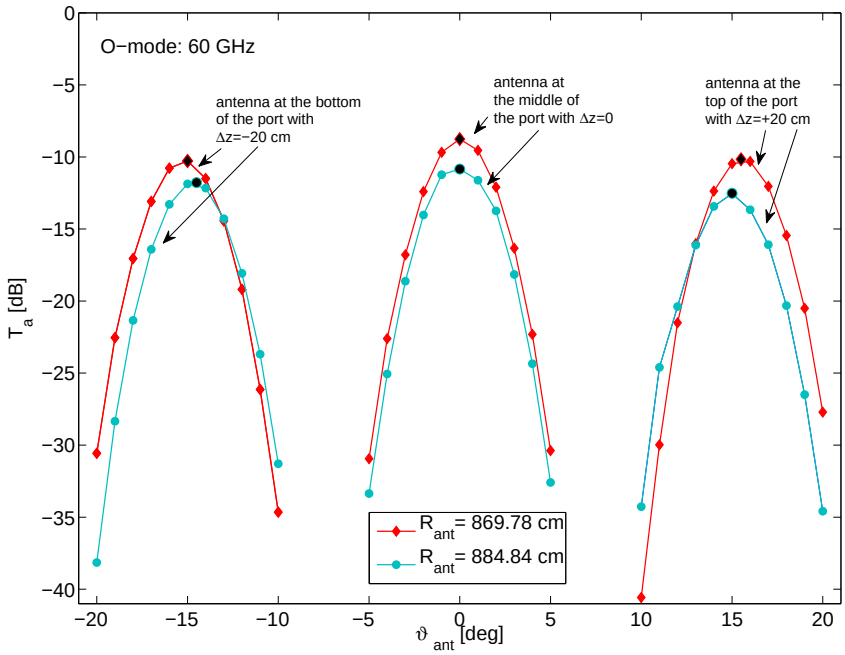

Figure 3.6: Coupling efficiency T_a as function of the poloidal tilt angle ϑ_{ant} of a 60 GHz O-mode beam at $z = 0.62$ m (middle of the port with $\Delta z = 0$), $z = 1.72$ m (top of the port with $\Delta z = +0.20$ m) and $z = -0.48$ m (bottom of the port with $\Delta z = -0.20$ m), and $R_{ant} = 8.6978$ m (0.20 m recess) as well as $R_{ant} = 8.8478$ m (0.35 m recess)

the bottom of the port. The middle of the port serves as reference to the previous figures. Recessing the antenna to $R_{ant} = 8.8478$ m (mirror configuration) leads to a decrease of the power coupling within a range of 2.5 dB in comparison to $R_{ant} = 8.6978$ m. The decrease is due to the longer path lengths which result in the beam expanding more and therefore a spreading of the reflected power. As well, the optimal tilt is roughly 0.5° less with the 0.35 m recess. As discussed above, coupling is best for an incoming beam perpendicular to the cutoff layer. Therefore slightly smaller tilt angles are needed at larger recesses to achieve optimal coupling.

Fig. 3.6 and Fig. 3.7 show that, apart from absolute values, the structure of the dependence of the coupling efficiency on the poloidal tilt angle is the same at all positions and recesses at each frequency. With the aid of Fig. 3.3 and Fig. 3.4, this tendency can be extended by other frequencies. Together with Fig. 3.1 and Fig. 3.2, this leads to an overall picture, where the 3 dB sensitivity width is independent of antenna placement, e.g. height and recess.

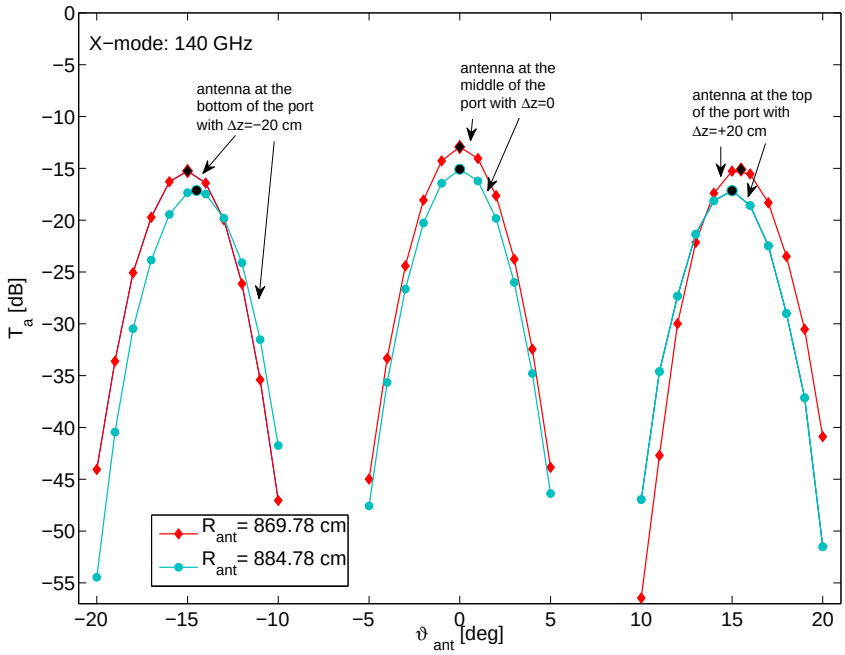

Figure 3.7: Coupling efficiency T_a as function of the poloidal tilt angle ϑ_{ant} of a 140 GHz X-mode beam at $z = 0.62$ m (middle of the port with $\Delta z = 0$), $z = 1.72$ m (top of the port with $\Delta z = +0.20$ m) and $z = -0.48$ m (bottom of the port with $\Delta z = -0.20$ m), and $R_{ant} = 8.6978$ m (0.20 m recess) as well as $R_{ant} = 8.8478$ m (0.35 m recess)

3.2 Part Two: Time Evolution of the Plasma

Previous investigations of the performance of ITER reflectometers were based on a single time slice of an ITER discharge, usually corresponding to the end of the burn phase. However, it is crucial to assess the potentiality for the reflectometry system of diagnosing the whole time evolution of the discharge. To achieve this, equilibria for the whole plasma discharge are required. For this thesis, the required equilibria were available for the first time.

To calculate the equilibria, the MHD-equations (MHD = MagnetoHydroDynamics) are used. As mentioned in section 1.3, the plasma is confined due to a magnetic field. In this case, the equilibrium of forces is given by the modified MHD equation:

$$\nabla p = \vec{j} \times \vec{B}, \tag{3.1}$$

which means that the pressure gradient in the plasma is balanced by the currents and magnetic fields in the plasma according to the Lorentz force. Solving this equation allows the

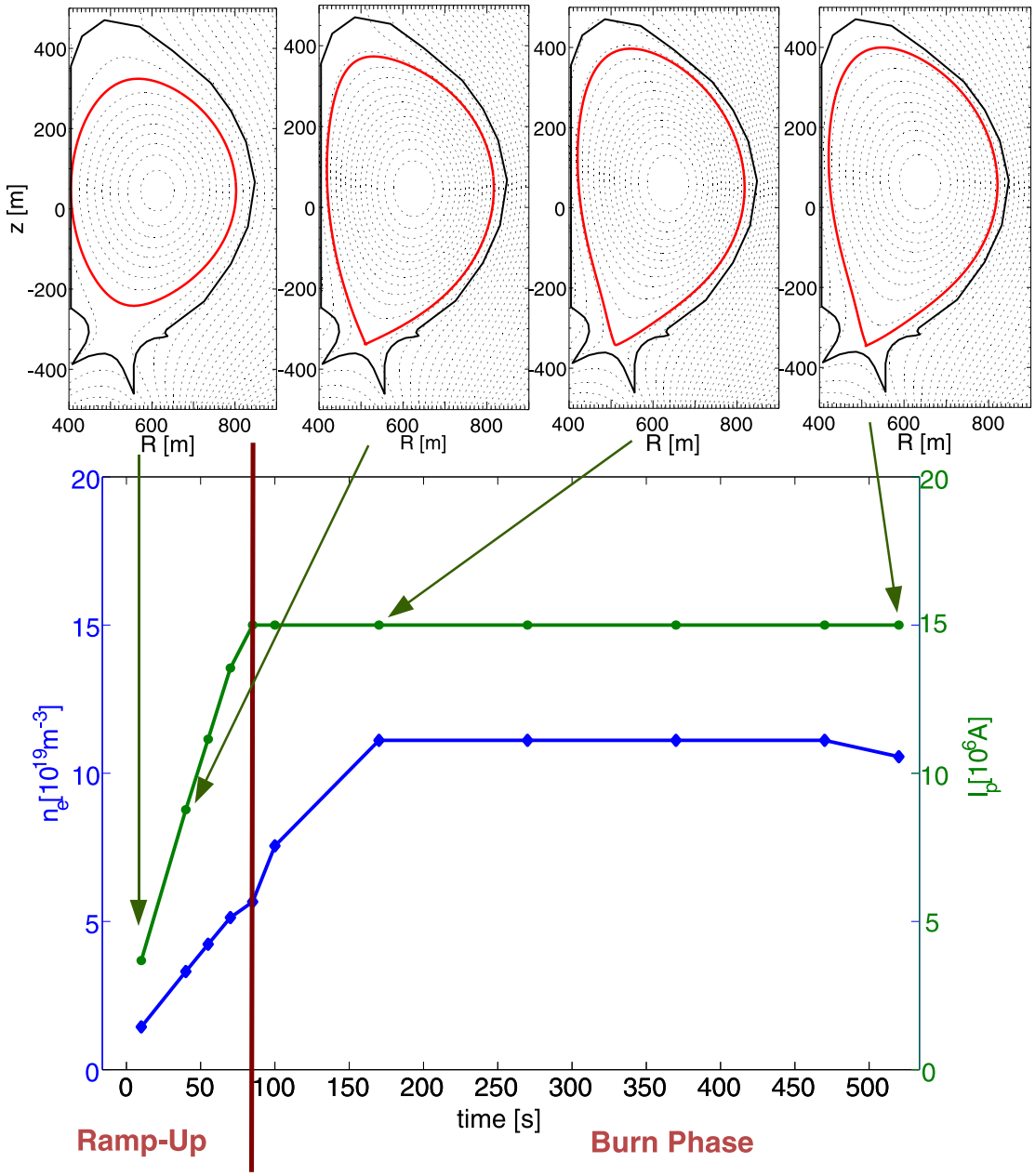

Figure 3.8: Evolution of the maximum electron density n_e and the plasma current I_p as functions of the time over ramp-up and burn phase of the plasma discharge. On the top, the poloidal cross sections illustrate, how the separatrix and the flux surfaces evolve at different time steps.

determination of the flux surfaces. With the aid of assumptions about the transport, density and temperature profiles are calculated such as to satisfy the ideal gas law $p = nk_BT$.

The equilibria used are generated with the aid of the equilibrium solver CREATE – NL [29], which is coupled to the transport solver JINTRAC [30].

Fig. 3.8 shows the time evolution of the central electron density and the plasma current during the ramp-up and the burn phase for the equilibria time points t =10, 40, 55, 70, 85, 100, 170, 270, 370, 470 and 520 s. Above the figure, the poloidal cross section of the ITER tokamak is shown for the selected time points of $t = 10, 40, 170$ and 520 s. From this figure, it can be seen that the final form of the plasma (as it is already known from the end of the burn phase (see Fig. 2.3 a)) is achieved fairly quickly during the ramp-up phase. The X-point is already formed at 40s. After this, the main modification with respect to the form is given by the flux surfaces being pushed outwards. However, the different parameters evolve at different rates. The core electron density rises a lot slower and only reaches its constant maximum at about 170s, while the plasma current is constant after 85s whereafter the burn phase starts. The differing pace of the parameter evolutions is important for the discussion of reflectometry results.

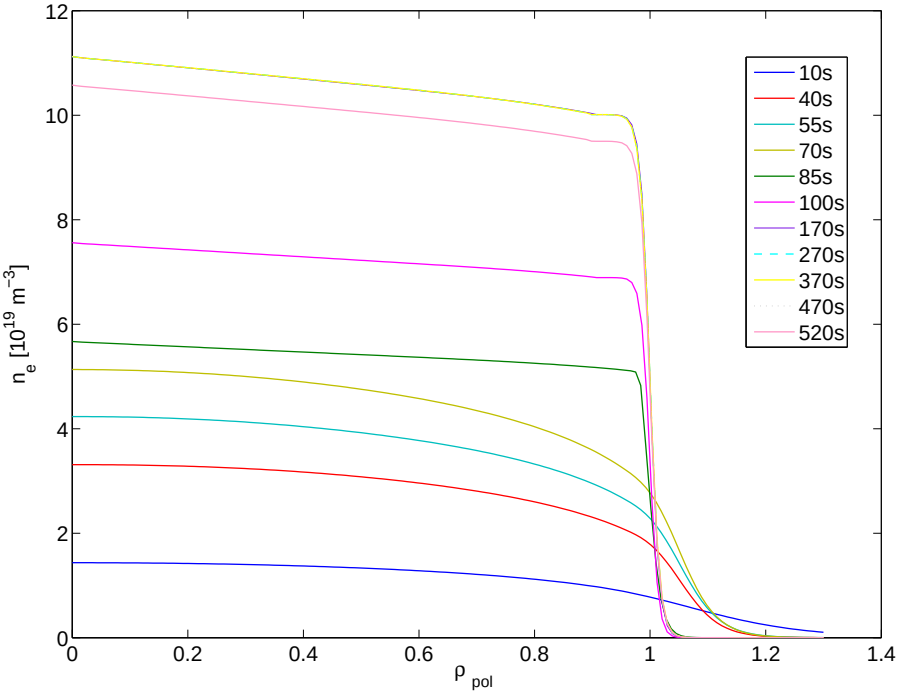

Figure 3.9: Time evolution of the electron density profile as a function of ρ_{pol} from the beginning of the ramp-up to the end of the burn phase

In Fig. 3.9, the time evolution of the density profile during the ramp-up and burn phase is shown. The density profiles have been extrapolated at the edge of the plasma to provide a smooth monotonic profile for the beam tracing. The profiles have been fitted with a tanh

(hyperbolic tangent) function to have a first guess of the scrape-off-layer density. The build up of the density profile, which is in accordance to Fig. 3.8, starts quickly, then slows down. In between 170 an 470s, the density profile is constant and starts to fall again at the end of the burn phase. The form of the density profile begins from a low smooth L-mode profile and evolves into the H-mode (see Fig. 2.3 d)) profile with the steep edge pedestal and almost constant flat core, at around 85s.

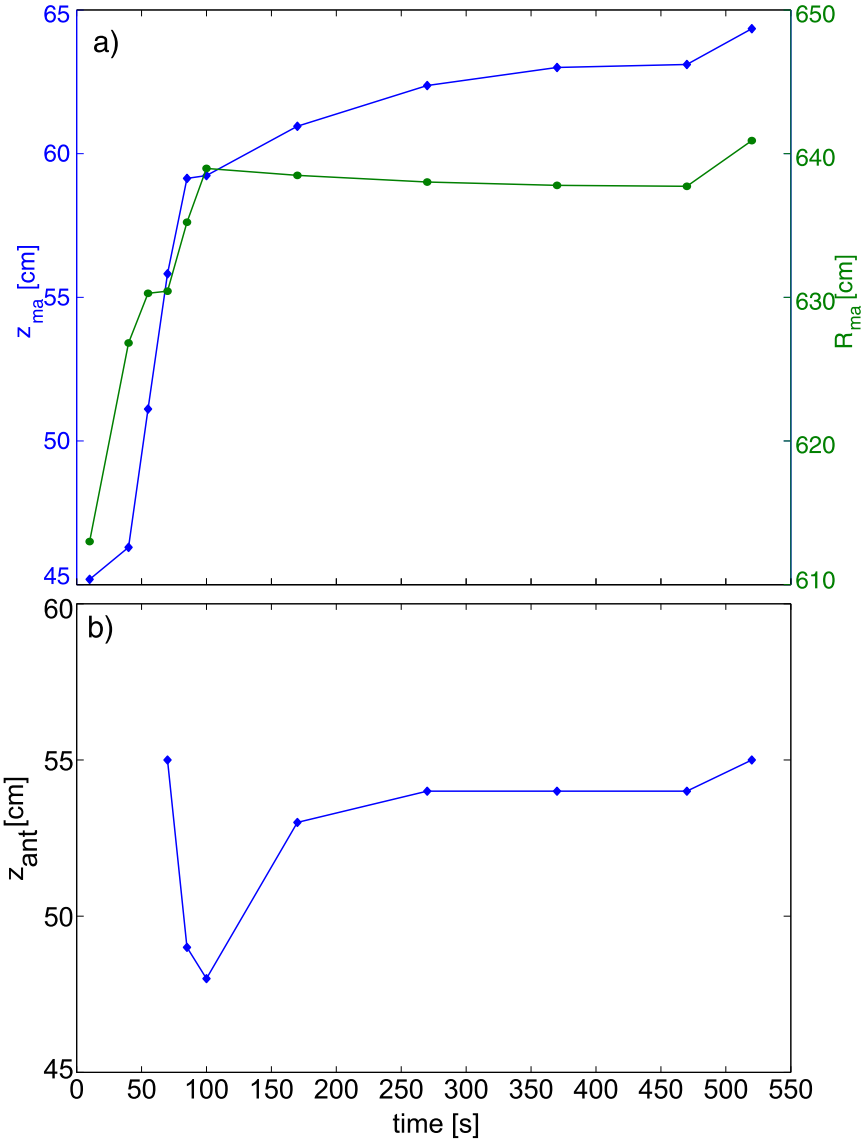

Figure 3.10: a) Evolution of the plasma magnetic axis position, given by its coordinates R_{ma} and z_{ma}, and b) optimal height of a horizontal aligned antenna z_{ant} for $\vartheta_{ant} = 0°$ and $R_{ant} = 8.6978$ m for 60 GHz O-mode beam as functions of time during the ramp-up and the burn phase of the plasma discharge

In Fig. 3.10 a), the evolution of the plasma magnetic axis is shown with the coordinates R_{ma} and z_{ma} plotted as a function of time. The magnetic axis moves rapidly during the ramp-up and continues to evolve during the burn phase. Particularly, the height of the magnetic axis still increases significantly.

Fig. 3.10 b) shows the optimal (horizontally aligned $\vartheta_{ant} = 0°$) antenna height z_{ant} as a function of time for the 60 GHz O-mode beam at $R_{ant} = 8.6978$ m. This essentially simulates the required performance of a vertical array of fixed tilt antennas. There are two main points: firstly, as the density is too low, there is no reflection before $t = 55$ s and secondly, the bend of the curve with the minimum at $t = 100$ s, due to the shape change of the edge flux surfaces up to 100 s and then the vertical movement of the plasma column.

As discussed in section 3.1, the antenna system can be placed at different positions. However, the middle of the port as initial position for examination is reasonable. Here, an antenna with steerable tilt was placed at $z_{ant} = 0.62$ m and $R_{ant} = 8.6978$ m. The development of the plasma was traced by varying the poloidal tilt angle from this fixed position instead of moving the antenna up and down as it was done before. Fig. 3.11 shows the optimal poloidal tilt angle as a function of time for the O-mode frequencies 18, 60 and 80 GHz and the X-mode frequencies 120, 140 and 160 GHz. It is seen that for all frequencies, except for the 18 GHz O-mode, the beams are not reflected at the beginning of the discharge. As Fig. 3.9 shows, the density and consequently the plasma frequency is too low at the beginning of the plasma discharge. As the cutoff condition for the O-mode is $\omega_p = \omega$, for each frequency there is a minimum density for reflection. However, cutoff conditions for X-mode polarization are as well dependent on the magnetic field. Consequently, although the probe frequencies are higher than for O-mode, reflection starts earlier. Another distinctive feature of Fig. 3.11 is the bend at $t = 70$ s for all investigated frequencies. This is probably a consequence of the fact that shape change and z_{ant} effects are in opposite directions. ϑ_{opt} shows a different evolution to $z_{ant,opt}$ since it can follow the cutoff inclination more closely than with a pure horizontal antenna.

As a consistency check, it is important to compare the overall coupling efficiency T_a values using the new equilibria, with the original equilibrium in section 3.1. Generally, the coupling values T_a for the later burn phase (100 s to 520 s) are consistent between both equilibria. However, in some cases during the ramp-up, the coupling drops noticeably. This may be due to the flat density profile leading the beam to being reflected in the core of the plasma, and thus a longer path length, greater beam spread and consequently reduced T_a.

It should be noted that there were problems with the beam tracing code for the 160 GHz X-mode, i.e. very long propagation path lengths resulting in the absence of points for the 160 GHz X-mode case for $t < 170$ s in Fig. 3.11.

Unfortunately, due to time constraints, it was not possible to fully assess the 3 dB sensitivity range of the optimal tilt during the plasma evolution. Nevertheless, the frequency (e.g.

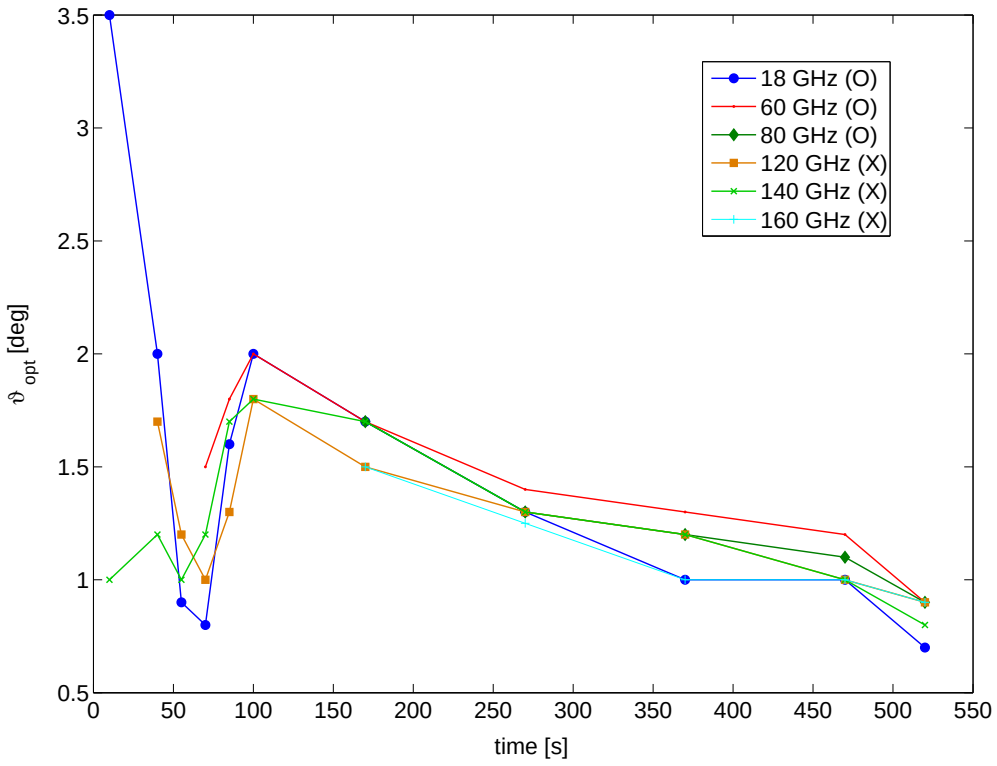

Figure 3.11: Optimal poloidal tilt angle ϑ_{ant} as a function of the time for the O-mode beam frequencies 18, 60 and 80 GHz, as well as the X-mode beam frequencies 120, 140 and 160 GHz at $R_{ant} = 8.6978$ m and $z_{ant} = 0.62$ m

antenna gain) dependency, shown in Fig. 3.5, will apply, namely the tilt variation is less critical for lower frequencies since they cause wider beam divergences.

3.3 Summary and Conclusions

The simulation exercises conducted throughout this work had the aim of investigating two main questions. The first one was to examine the ability of a steerable mirror or a mechanically tiltable antenna configuration to handle the plasma column vertical movement. It was determined that the $\Delta z = \pm 20$ cm vertical plasma variation can be compensated by $\Delta\vartheta = \pm 3°$, irrespective of the antenna placement in the port, the launch frequency and the polarization of the beam. Furthermore, it was shown that the half power (i.e. 3 dB) sensitivity is in the range of $\Delta\vartheta = 12°$ to $2°$ from the bottom to the top of the frequency bound for the investigated low gain antennas. The second aim was to investigate how much a steerable antenna needs to move to accommodate changes in the plasma equilibrium shape

and position during the plasma formation ramp-up and burn phase. Two approaches were considered here. It was examined how much a horizontally aligned antenna needs to move from $z = 0.62$ m and how much a fixed antenna at $z = 0.62$ m needs to be tilted in order to track the evolution. In the first case, the plasma evolution is accommodated in between $\Delta z_{ant} = 7$ cm and 12 cm (ramp-up) and $\Delta z_{ant} = 13$ cm and 7 cm (burn phase). In the second case, the optimal antenna tilt is between $\vartheta_{ant} = 3.5^\circ$ and 0.8°, i.e. $\Delta\vartheta = 2.7^\circ$ (ramp-up) and $\vartheta_{ant} = 2.0^\circ$ and 0.7°, i.e. $\Delta\vartheta = 1.3^\circ$ (burn phase).

This leads to the conclusion that a steerable antenna system could easily compensate both vertical displacements during the burn phase and equilibrium variations during the ramp-up and burn phase of the plasma discharge. This study, as with previous studies, confirm that a ±20 cm vertical plasma column movement could be accommodated with a single antenna system of sufficiently low gain (e.g. 'wide beam divergence'). However, there are significant benefits to be gained by using a high gain (less divergent) antenna - for example core plasma probing at higher frequencies and overall higher T_a coupling values. Here, a single steerable high gain antenna has many advantages over a vertical antenna array, including a saving in cost, hardware and space, but at the expense of additional antenna sophistication. For deeper core probing, using only a single antenna would generally not be possible without tilting. Throughout this thesis, two possible steerable systems were considered: one, based on mechanical tilting of the waveguide at a recess of 20 cm, and the other, more realistically, via a mechanically controlled reflector element (e.g. mirror). Both options are technically realizable and could achieve the desired tilt/scan range and accuracy with sufficient time/dynamic control, consistent with the slow (e.g. 100 ms) time evolution of the equilibrium.

Bibliography

[1] B. Povh, K. Rith, C. Scholz, and F. Zetsche, Particles and Nuclei, Berlin: Springer Verlag, 4th ed., (2004).

[2] U. Schuhmacher, Fusionsforschung, Darmstadt: Wissenschaftliche Buchgesellschaft, (1993).

[3] J. Wesson, Tokamaks, New York: Oxford University Press, 3rd. ed., (2004).

[4] T. H. Stix, Waves in Plasmas, New York: AIP, (1992).

[5] D. G. Swanson, Plasma Waves, Series in Plasma Physics, Bristol: Institute of Phyiscs Publishing, 2nd ed., (2003).

[6] M. Young, Optik, Laser, Wellenleiter, Berlin: Springer Verlag, (1993).

[7] G.V. Pereverzev, Paraxial WKB solution of a scalar wave equation, in: Reviews of Plasma Physics 19 (B.B. Kadomtsev, ed.), Consultants Bureau, (1996).

[8] G.V. Pereverzev, Beam tracing in inhomogeneous anisotropic plasmas, Phys. Plasmas, Vol. 5, p. 3529, (1998).

[9] E. Poli et al., Paraxial Gaussian wave beam propagation in an anisotropic inhomogeneous plasma, Phys. Plasmas, Vol. 6, p. 5, (1999).

[10] E. Poli, Diffraction effects on electromagnetic gaussian beams in anisotropic inhomogeneous plasmas, PhD thesis, Universitá degli Studi di Pavia, (1998).

[11] E. Poli et al., TORBEAM, a beam tracing code for electron-cyclotron waves in tokomak plasmas, Comp. Phys. Comm., Vol. 136, p. 90, (2001).

[12] E. Mazzucato, Relativistic effects on microwave reflectometry, Phys. Fluids B, Vol. 4, p. 3460, (1992).

[13] O. Maj et al., Validation of the paraxial beam-tracing method in critical cases, Phys. Plasmas, Vol. 16, 062105, (2009).

[14] O. Maj et al., Effects of aberration on paraxial wave beams: beam tracing versus quasi-optical solutions, Plasma Phys. Control. Fusion, Vol. 52, p. 085006, (2010).

[15] I. H. Hutchinson, Principles of plasma diagnostics, Cambridge: Cambridge University Press, (1987).

[16] G. D. Conway, Microwave reflectometry for fusion plasma diagnosis, Nucl. Fusion, Vol. 46, pp. S665-S669, (2006).

[17] C. Laviront et al., Reflectometry techniques for density profile measurements on fusion plasmas, Plasma Phys. Control. Fus., Vol. 38, pp. 905-936, (1996).

[18] M. E. Manso, Reflectometry in fusion devices, Plasma Phys. Control. Fus., Vol. 35, pp. B141-B155, (1993).

[19] V. S. Udintsev, System Design Description Document (DDD) Diagnostic - Low Field Side Reflectometry DDD-PBS 55.F2, ITER_D_47QCBN, (2011).

[20] A. Stegmeir, G. D. Conway, E. Poli, E. Strumberger, Analysis of the ITER low field side reflectometer employing the Beam Tracing Method, Fus. Eng. Des., Vol. 86, pp. 2928, (2011).

[21] S. Silver and H. M. James, eds., Microwave Antenna Theory and Design. IEE Electromagnetic Wave Series 19, London: Peter Peregrinus Ltd, (1984).

[22] G. Vayakis et al., Status and prospects for mm-wave reflectometry in ITER, Nucl. Fusion, Vol. 46, pp. S836-S845, (2006).

[23] G. Wang et al., Refractive and relativistic effects on ITER low field side reflectometer design, Rev. Sci. Instrum., Vol. 81, 10D908, (2010).

[24] G. D. Conway et al., Antenna configuration options for the ITER low-field-side LFS reflectometer, ITER_D_35AHBB, (2011).

[25] G. J. Kramer et al., 2D reflectometer modelling for optimizing the ITER low-field side X-mode reflectometer system, Nucl. Fusion, Vol. 46, pp. S846-S852, (2006).

[26] A. Stegmeir, Anwendung der Beam Tracing Methode zur Diagnostik von Fusionsplasmen, Dipl. thesis, Technische Universität München, (2010).

[27] G. Vayakis and L. Zabeo, Z-range of ITER plasmas for LFS reflectometry, Presentation at ITER_D_3TFDLN, (November 2010).

[28] M. A. Henderson et al., Overview of the ITER EC upper launcher, Nucl. Fus., Vol. 48, 054013, (2008).

[29] S.Wiesen, JINTRAC JET modelling suite, http://www.eirene.de/JINTRAC_Report_2008.pdf, (2008).

[30] R. Albanese, G. Calabrò, M. Mattei, and F. Villone, Plasma Response Models for Current, Shape and Position Control in JET, Fus. Eng. Des, Vol. 66-68, pp. 715-718, (2003).